

Mg-Doped MnO₂ Cathode with Tailored Oxygen Vacancies for High-Rate High-Capacity Calcium Storage

Gege Li, Wei Huang, Lu Xue, Chi-Pong Tsui, Yalong Jiang,* Chak-Yin Tang, and Yingkui Yang*

Calcium-ion batteries are promising candidates for next-generation energy storage systems due to their high output voltage, abundant calcium resources, and intrinsic safety. Among various cathode materials, MnO₂ stands out for its low cost, environmental friendliness, and high energy density. However, its practical application is limited by poor conductivity and structural instability arising from the Jahn-Teller distortion of Mn(III)O₆ octahedra. Herein, Mg-doped MnO₂ nanosheets grown on carbon cloth are synthesized via a one-step hydrothermal method to overcome these limitations. Mg doping introduces oxygen vacancies that alleviate Jahn-Teller distortion by modulating the local electronic

environment and further enhances structural stability. Additionally, the enlarged interlayer spacing weakens the electrostatic interactions with Ca²⁺ ions, thereby promoting rapid ion diffusion. As a result, the optimized electrode delivers a high reversible specific capacity (458.2 mAh g⁻¹ at 0.1 A g⁻¹), excellent rate capability (164.2 mAh g⁻¹ at 1 A g⁻¹), and cycling stability (99.3% capacity retention after 1000 cycles at 1.0 A g⁻¹). Ex situ analyses reveal a cointercalation mechanism involving both H⁺ and Ca²⁺ ions. This work offers a defect-engineering strategy for developing high-performance cathode materials.

1. Introduction

Lithium-ion batteries have dominated the electrochemical energy storage market, including portable electronics, electric vehicles, and smart grids, due to their superior cycle life and energy density. However, the surging lithium resource consumption has driven the urgent exploration of more cost-effective alternatives.^[1–3] Multivalent metal-ion batteries, leveraging multi-electron redox reactions, emerge as promising candidates for next-generation energy storage systems owing to their theoretically superior energy density and cost-effectiveness.^[4] Calcium-ion batteries (CIBs) have attracted considerable attention due to their unique physicochemical advantages. The Ca²⁺/Ca redox couple possesses a notably low standard reduction potential

(−2.87 V vs. standard hydrogen electrode (SHE)), comparable to that of Li⁺/Li (−3.04 V vs. SHE), thereby enabling high operating voltage and energy density.^[5,6] Moreover, the low charge density of Ca²⁺, the dendrite-free deposition/stripping behavior, and the abundance of calcium as the fifth element in the Earth's crust collectively contribute to the superior rate capability, cost-effectiveness, and intrinsic safety of CIBs.^[7]

To achieve high-performance CIBs, the development of efficient cathode materials remains a central research focus. Various cathode materials have been explored, including Prussian blue and its analogs, metal oxides, metal sulfides, polyanionic compounds, and organic materials.^[8] Among these, manganese dioxide (MnO₂) shows great application prospects due to its low cost, environmental friendliness, high energy density, and suitable operating voltage. In particular, δ-MnO₂, with a unique layered structure and large interlayer spacing, is conducive to facilitating rapid ion diffusion and demonstrates promising potential in energy storage applications. However, its inherently low electronic conductivity^[9,10] and structural instability caused by the Jahn-Teller distortion of Mn (III)O₆ polyhedra^[11–16] remain critical challenges. In addition, the large ionic radius and relatively high charge density of Ca²⁺ lead to strong electrostatic interactions with the MnO₆ octahedral layers, further resulting in sluggish ion diffusion kinetics.^[8–10] To address these challenges, various optimization strategies have been proposed in recent years, including ion doping, nanotechnology, and defect engineering.^[17–19] Metal cations doping, including K, Zn, Cu, Mg, Al, and Mo,^[20–25] as one of the effective strategies, can improve the ion/electron transport kinetics and structural stability of δ-MnO₂ cathodes by enhancing local electric fields and tuning the electronic structure through the introduction of oxygen vacancies.^[26,27] Wang et al. introduced oxygen defects into the δ-MnO₂ framework by Cu²⁺ doping, which

G. Li, L. Xue, Y. Jiang, Y. Yang

State Key Laboratory of New Textile Materials and Advanced Processing

Wuhan Textile University

Wuhan 430200, China

E-mail: yjiang@wtu.edu.cn

ykyang@wtu.edu.cn

W. Huang

School of Chemistry and Materials Science

South-Central Minzu University

Wuhan 430074, China

C.-P. Tsui, C.-Y. Tang

Department of Industrial and Systems Engineering

The Hong Kong Polytechnic University

Hung Hom, Kowloon, Hong Kong, China



Supporting information for this article is available on the WWW under <https://doi.org/10.1002/batt.202500331>



© 2025 Wiley-VCH GmbH. This is an open access article under the terms of the Creative Commons Attribution License, which permits use, distribution and reproduction in any medium, provided the original work is properly cited.

facilitated charge transfer and enhanced Zn^{2+} reaction kinetics. As a result, the Cu-doped δ - MnO_2 delivered a high reversible capacity of 296.8 mAh g $^{-1}$ and exhibited a desirable rate capability.^[28] Suib et al. reported Zn-doped δ - MnO_2 electrode materials for zinc-ion storage, which modified the microstructure and enhanced the reaction kinetics, resulting in an ultrahigh reversible capacity of 455 mA h g $^{-1}$ and an excellent specific energy of 628 Wh kg $^{-1}$.^[29] Besides, Sun et al. has reported the use of high-valent metal cation Al as a dopant to prepare Al-doped δ - MnO_2 by an electrochemical oxidation method. The abundant Al cation vacancies provide 3D diffusion channels for zinc-ion storage, while the doped Al could improve the structural stability by suppressing the Jahn-Teller distortion of Mn (III)O₆ polyhedra during cycling, resulting in the superior rate performance (135.8 mA h g $^{-1}$ at 8 A g $^{-1}$) and high capacity retention (87% after 1000 cycles at 1 A g $^{-1}$).^[21] Although these methods address certain issues reported previously, such as sluggish ion diffusion kinetics and structural instability, further improvement in reaction kinetics is still required by enhancing electron conductivity. To the best of our knowledge, doping with cations of relatively high electronegativity can enhance the intrinsic conductivity by introducing oxygen vacancies.^[30] Mg ion with relatively high electronegativity has been used as dopant to further improve the electrochemical performance of

MnO_2 . Xu et al. synthesized Mg-doped MnO_2 @carbon cloth with increased vacancies for supercapacitors, resulting in an expanded voltage window of 0–1.2 V and high areal specific capacitance of 1088 mF cm $^{-2}$.^[31] Xia et al. reported a Mg-doped MnO_2 electrode with optimized electrical conductivity through the introduction of cations and oxygen vacancies. Furthermore, the presence of Mg $^{2+}$ helps maintain the structural stability of the framework, which is beneficial for improving electrochemical performance during long-term cycling. However, Mg-doped MnO_2 has not yet been reported in CIBs, and its electrochemical performance and reaction mechanism remain unclear and require further investigation.

Herein, Mg-doped MnO_2 nanosheets grown on carbon cloth (MMO) have been synthesized via a one-step hydrothermal method as a cathode material for CIBs. As illustrated in Figure 1a, the introduction of Mg into MnO_2 generates oxygen vacancies, which not only alleviates the Jahn-Teller distortion of Mn (III)O₆ polyhedra by tuning the local electronic structure of Mn, thus enhancing structural stability, but also enlarges the interlayer spacing of MnO_2 , reducing the local electrostatic interaction between Ca $^{2+}$ ions and the MnO₆ polyhedral layers, thus promoting rapid ion diffusion. Kinetic analyses reveal that the MMO electrode with a high concentration of oxygen vacancies exhibits fast electrochemical reaction kinetics. As a result, the

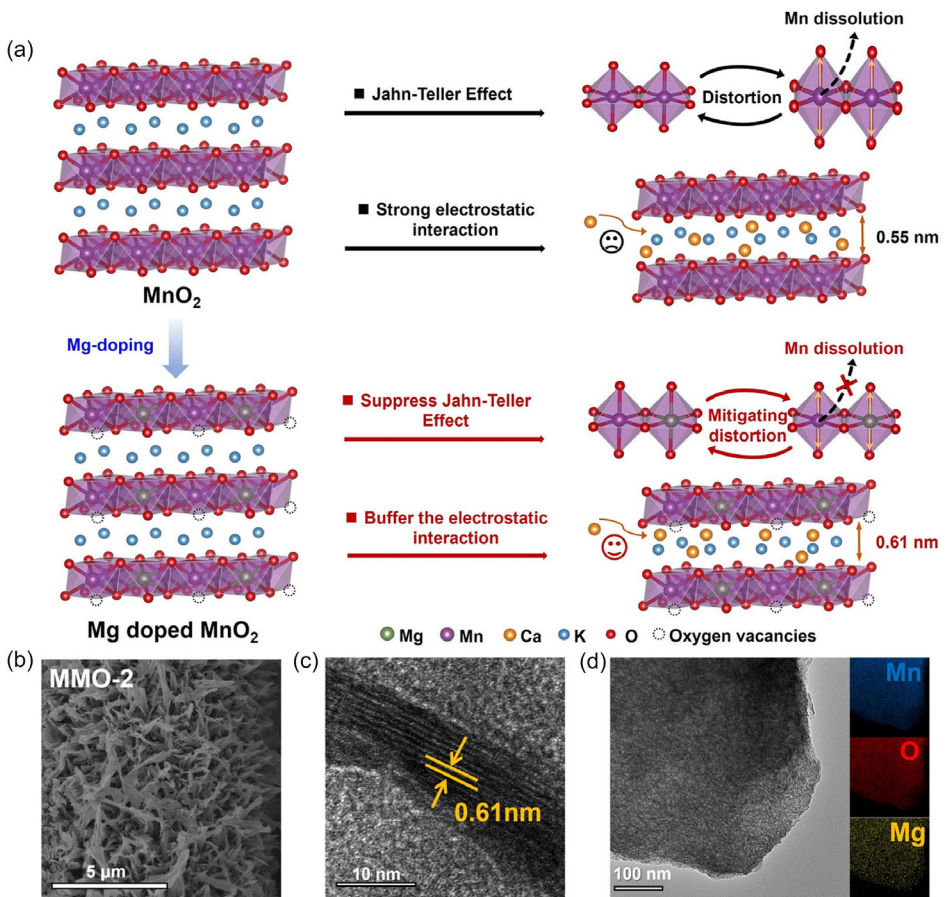


Figure 1. a) Schematic illustration of the Mg-doped strategy for optimizing the calcium storage performance of MnO_2 . MMO electrode effectively promotes ion diffusion and suppresses the Jahn-Teller effect. b-d) SEM, HRTEM images, and EDS mappings of MMO-2.

optimized MMO electrode delivers the excellent electrochemical performance. Furthermore, the electrochemical reaction mechanism of MnO_2 was investigated through ex situ characterizations. This work provides a defect-engineering strategy for the design of high-performance cathode materials.

2. Results and Discussion

The MMO samples were synthesized via a one-step hydrothermal method (Figure S1, Supporting Information). The Mg content in MMO was tuned by changing the MgCl_2 amount, with the samples labeled MMO-1, MMO-2, and MMO-3. The MnO_2 without Mg doping was labeled MO as a control. Scanning electron microscopy (SEM) images reveal that all samples exhibit a uniform nanosheet morphology, and varying Mg doping levels do not alter the overall structure of the MMO samples (Figure 1b, S2–S4, Supporting Information). High-resolution transmission electron microscopy (HRTEM) images further provide insights into the microstructure of the samples. As shown in Figure S2b, Supporting Information, the MO sample exhibits good crystallinity, and the interplanar spacing of 0.55 nm corresponds to the (001) crystal plane. After Mg^{2+} doping, the interplanar spacing of the (001) crystal plane in the MMO samples increased to 0.61 nm (Figure 1c), which may be attributed to the weakened interactions between MnO_6 polyhedral layers due to the modulation of the local electronic structure by Mg doping.^[32] In addition, energy-dispersive X-ray spectroscopy (EDS) mapping results show a uniform distribution of Mg, Mn, and O elements in MMO-1, MMO-2, and MMO-3,

indicating that Mg is homogeneously doped into the MnO_2 (Figure 1d and S3c, S4c, Supporting Information).

Based on the inductively coupled plasma analysis, the actual Mg doping contents in the MMO-1, 2, and 3 are 0.06%, 0.08%, and 0.25%, respectively (Figure S5, Supporting Information). X-ray diffraction (XRD) analysis further confirmed the phase composition of the obtained samples (Figure 2a). The diffraction peaks of all samples are in good agreement with the characteristic peaks of $\delta\text{-MnO}_2$ (JCPDS No. 80-1098). No impurity peaks were observed in the MMO samples, indicating that Mg ions were successfully incorporated into the MnO_2 lattice structure.^[20,30,33] According to Bragg's law, the (001) peak of MMO samples shifts slightly to a lower angle compared to that of the MO sample, indicating an increase in the interlayer spacing, which is consistent with the HRTEM results.^[34,35] The enlarged interlayer spacing can reduce the local electrostatic interaction between Ca^{2+} ions and MnO_6 polyhedral layers, thereby facilitating ion diffusion.^[36,37] Raman spectroscopy was employed to investigate the molecular structure of the samples by analyzing the vibrational and rotational energy levels of chemical bonds (Figure 2b). The Raman shift at 530–650 cm^{-1} corresponds to the stretching vibration peak of the Mn–O bond. Compared to the MO sample, the Raman peaks of the MMO samples shift to higher wavenumbers with significantly reduced intensities, indicating that Mg doping in MnO_2 induces the formation of oxygen vacancies.^[38] These oxygen vacancies are generated as Mg^{2+} partially replaces Mn^{4+} in MnO_2 , leading to charge imbalance and weakened metal–oxygen bonds. To maintain charge neutrality, oxygen vacancies form within the crystal lattice.^[39,40] The N_2 adsorption–desorption curves show a typical type III isotherm, corresponding to macropores or open

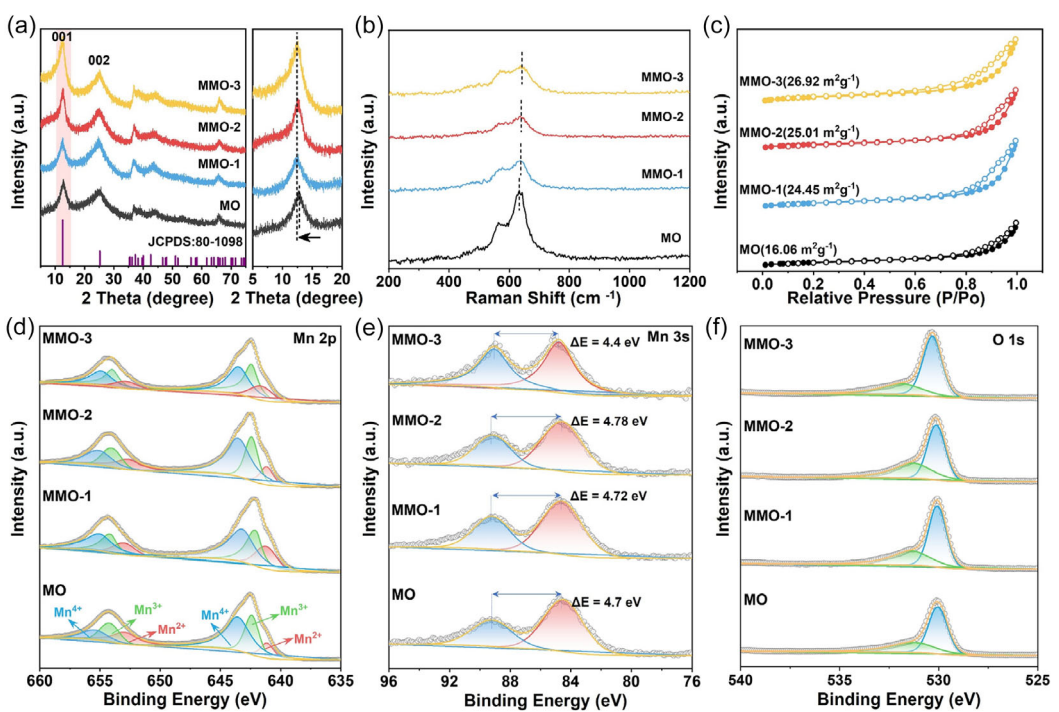


Figure 2. a–c) XRD patterns, Raman spectra, N_2 adsorption–desorption isotherms, and specific surface area of MO and MMO samples. d–f) Mn 2p, Mn 3s, and O 1s XPS spectra of MO and MMO samples.

pore structures (Figure 2c). The Brunauer–Emmett–Teller specific surface area of the MMO samples (24.45, 25.01, and 26.92 m² g⁻¹) is higher than that of the MO sample (16.06 m² g⁻¹), which increases the contact area between the electrode and electrolyte, thereby exposing more active sites. The surface chemical compositions of the samples were further analyzed using X-ray photoelectron spectroscopy (XPS). The Mn 2p XPS spectra of the samples are shown in Figure 2d, with Mn 2p_{1/2} and Mn 2p_{3/2} peaks observed at 654.3 and 642.5 eV, respectively. The high-resolution Mn 2p XPS spectra reveal the presence of mixed valence states, including Mn⁴⁺, Mn³⁺, and Mn²⁺.^[41–43] In the Mn 3s XPS spectra of the obtained samples, the binding energy difference (ΔE_s) between the main peak and the oscillation peak for MO, MMO-1, MMO-2, and MMO-3 is 4.70, 4.72, 4.78, and 4.40 eV, respectively (Figure 2e). Based on these ΔE_s values, the average oxidation states of Mn in MO, MMO-1, MMO-2, and MMO-3 were calculated to be 3.639, 3.616, 3.549, and 3.978, respectively (Table S1, Supporting Information).^[44] With increasing Mg doping content, the Mn valence first decreases and then increases, which is attributed to the changes in the Mn–O coordination environment.^[45] These changes are induced by the formation of Mg–O bonds

and the generation of oxygen vacancies resulting from Mg doping.^[41] Figure 2f shows the O 1s XPS spectra of the samples. The main peak at 529.5 eV is attributed to lattice oxygen in metal oxides (Mn–O–Mn), while the peak at 531.22 eV corresponds to oxygen vacancies.^[35,46] Compared with MO, MMO samples exhibit a more intense oxygen vacancy peak, indicating a higher concentration of oxygen vacancies.^[47] In the Mg 1s XPS spectra of the samples (Figure S7, Supporting Information), a peak at 1303.6 eV is observed in the MMO samples, confirming the successful incorporation of Mg into δ -MnO₂. Electron paramagnetic resonance spectroscopy was performed to identify the presence of oxygen vacancies (Figure S6, Supporting Information). The symmetric peaks observed in MMO samples show stronger signal intensities at a g-factor of 2.003 than that of MnO₂, which can be attributed to unpaired electrons trapped at oxygen vacancies within the crystal lattice.^[48] These vacancies enhance the electronic conductivity of MMO, thereby contributing to the superior electrochemical performance. Among them, MMO-2 exhibits the strongest signal, indicating the highest concentration of oxygen vacancies.

A CR2032 coin-type cell was assembled to evaluate the electrochemical performance for Ca²⁺ storage. Figure 3a displays the

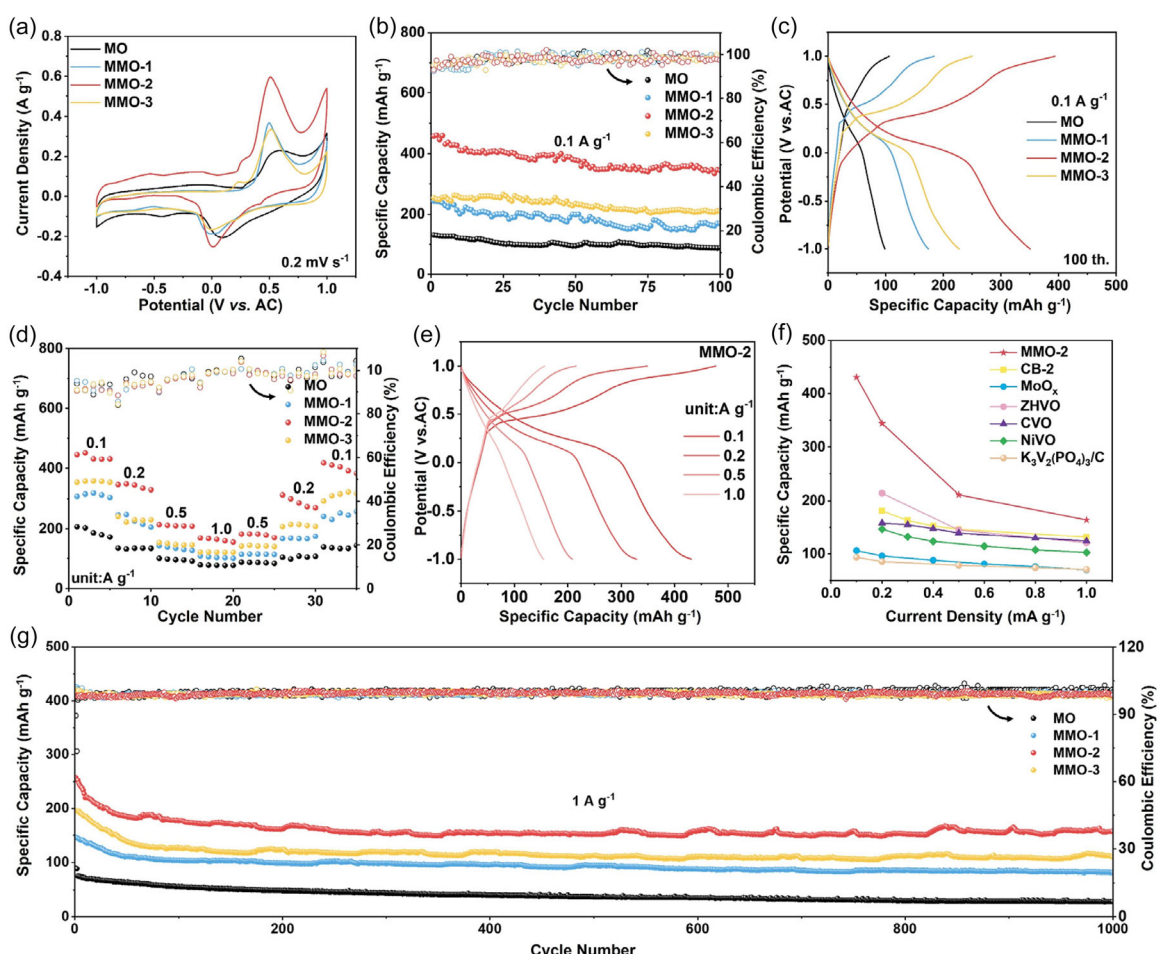


Figure 3. a–c) CV curves at 0.2 mV s⁻¹, cycling performance at 0.1 A g⁻¹, and the GCD curves at 0.1 A at 100th cycle of MO and MMO samples. d) Rate performance of MO and MMO samples. e) GCD curves of MMO-2 at different current densities. f) Comparison of rate performance between MMO-2 and reported cathodes for CLBs. g) Long-term cycling performance at 1 A g⁻¹ of MO and MMO samples.

cyclic voltammetry (CV) curves of the obtained samples measured at a scan rate of 0.2 mV s^{-1} within the potential window from -1.0 to 1.0 V versus AC. The MMO-2 (red curve) shows the highest current density, indicating that MMO-2 has a higher charge storage capacity. Further, the galvanostatic charge-discharge (GCD) curves of all samples at the 100th cycle show that MMO-2 delivers the highest specific capacities of 226.3 mAh g^{-1} and the smallest voltage hysteresis, indicating the fast reaction kinetics (Figure 3b). Figure 3c shows the cycling performance of MO and MMO samples at 0.1 A g^{-1} . Among the four samples, MMO-2 delivers the highest specific capacity of 458.2 mAh g^{-1} . Figure 3d shows the rate performance of all samples, with the MMO-2 electrode exhibiting superior rate capability. The specific capacities at 0.1 A g^{-1} are 431.4 mAh g^{-1} . Even at 1 A g^{-1} , a specific capacity of 164.2 mAh g^{-1} is maintained. When the current density is returned to 0.1 A g^{-1} , the specific capacity recovers to 410.9 mAh g^{-1} , indicating excellent reversibility. The GCD curves of the MMO-2 electrode at various current densities ranging from 0.1 to 1 A g^{-1} exhibit small polarization, indicating fast reaction kinetics (Figure 3e). Compared to the previously reported cathode materials, such as CB-2,^[49] MoO_x ,^[50] ZHVO,^[51] CVO,^[52] $\text{K}_3\text{V}_2(\text{Po}_4)_3/\text{C}$,^[53] and NiVO,^[54] MMO-2 exhibits the highest reversible capacity and superior rate performance (Figure 3f). Figure 3g shows the long-term cycling performance of MO and MMO samples at 1 A g^{-1} . After 1000 cycles, the reversible capacity of MMO-2 reaches 158.3 mAh g^{-1} , significantly higher than that of MO (only 28.6 mAh g^{-1}). This superior cycling stability is attributed to the introduction of Mg ion and oxygen vacancies into MnO_2 , which alleviates the Jahn-Teller distortion of Mn (III) O_6 polyhedra by

modulating the local electronic structure, thereby enhancing structural stability.^[55]

To elucidate the superior electrochemical performance of MMO electrodes, galvanostatic intermittent titration technique (GITT) and multiscan CV measurements were conducted to investigate the electrochemical reaction kinetics. GITT measurements were performed to analyze the Ca^{2+} diffusion kinetics (Figure 4a). Throughout the charge and discharge process, the calculated Ca^{2+} diffusion coefficient of MMO-2 was significantly higher than those of MO, MMO-1, and MMO-3 (Figure 4b), indicating faster Ca^{2+} migration and superior rate performance. In addition, the Nyquist plots of MO and MMO samples were obtained to evaluate the interfacial charge transfer resistance (R_{ct}), represented by the semicircle in the high-frequency region. As shown in Figure 4c, MMO-2 exhibits an R_{ct} value of 14.65Ω , which is significantly lower than those of the other three samples. The reduced charge transfer resistance facilitates faster electron transfer kinetics, thereby promoting Faradaic reactions at the electrode-electrolyte interface and enhancing overall electrochemical performance. Figure 4d,e and S8, Supporting Information, present the multiscan CV curves of MMO-2, MO, MMO-1, and MMO-3 at different scan rates. The contributions from capacitive behavior and ion diffusion can be quantified using the equation $i(V) = k_1v + k_2v^{1/2}$,^[56] where $i(V)$ is the current at a fixed potential V , k_1v represents the capacitive contribution, and $k_2v^{1/2}$ corresponds to the ion diffusion contribution. As shown in Figure 4f, the capacitive contribution of all samples increases with scan rate from 0.2 to 1 mV s^{-1} . Among them, MMO-2 exhibits the highest capacitive contribution, rising from 48.8% to 87.0% , indicating dominant

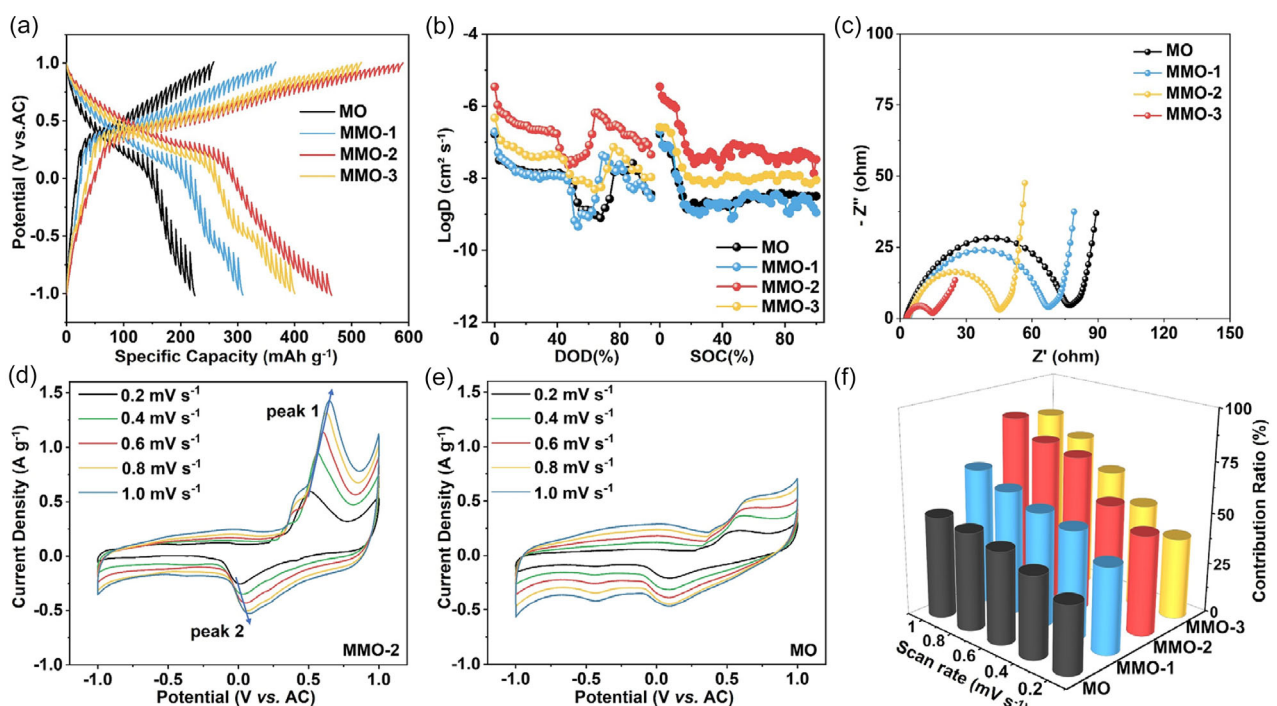


Figure 4. a,b) GITT curves and the corresponding calculated Ca^{2+} diffusion coefficients of MO and MMO samples. c) EIS spectra of the MO and MMO samples. d,e) CV curves of the MMO-2 and MO at various scan rates. f) Capacitive contributions of the MO and MMO samples at various sweep rates.

pseudocapacitive behavior that contributes to its superior rate capability.

To investigate the structural evolution and calcium ion storage mechanism of MMO-2 during the charge and discharge process, ex situ XRD, XPS, and HRTEM measurements were conducted at different charge and discharge states. Figure 5a, b shows the GCD curves for the first two cycles at 0.1 A g^{-1} and the corresponding ex situ XRD patterns of MMO-2. When discharged to -1.0 V versus AC, the diffraction peak of the (001) crystal plane shifts slightly to a lower degree, indicating an increase in interlayer spacing during ion insertion. Conversely, when charged to 1.0 V versus AC, the diffraction peak of the (001) crystal plane shifts back, indicating that the interlayer spacing shrinks during ion extraction. Compared to the pristine state, the Mn 2p XPS spectrum of MMO-2 in the discharged state shows a decrease in the $\text{Mn}^{4+}/\text{Mn}^{3+}$ ratio (Figure 5c). Upon charging, the $\text{Mn}^{4+}/\text{Mn}^{3+}$ ratio increases, indicating that the valence of the Mn element changes during the ion insertion and extraction processes. Figure 5d shows the Ca 2p XPS spectra during the discharging and charging process. The Ca 2p signal is detected in the discharge state and significantly reduced after charging, indicating the reversible Ca ions insertion/extraction processes. Figure 5e shows the HRTEM images of MMO-2 in both discharged and charged states. The interplanar spacing increases from the

initial 0.61 nm to 0.67 nm after discharging and returns to 0.61 nm upon charging. These results demonstrate the reversible ion insertion/extraction during the charge and discharge processes, consistent with the ex situ XRD results. Additionally, the EDS mapping of MMO-2 in the discharged state shows that Mn, O, Mg, and Ca elements are evenly distributed, indicating the successful insertion of Ca^{2+} ions (Figure 5f). Since a $2 \text{ M Ca (NO}_3)_2$ in a $\text{H}_2\text{O/AN}$ (4:1) mixture was used as the electrolyte, as reported in the literature, H^+ ions have also been inserted into MnO_2 .^[52] Based on this, the reaction mechanism of H^+ and Ca^{2+} cointercalation in MnO_2 has been proposed.

3. Conclusions

In summary, this study successfully synthesized Mg-doped MnO_2 nanosheets grown on carbon cloth via a one-step hydrothermal method as a cathode material for CIBs. The introduction of Mg into MnO_2 generates oxygen vacancies, which not only alleviates the Jahn-Teller distortion of $\text{Mn}(\text{III})\text{O}_6$ polyhedra by tuning the local electronic structure, thereby enhancing structural stability, but also enlarges the interlayer spacing of MnO_2 , reducing the local electrostatic interaction, thus facilitating fast ion diffusion. The MMO electrode with a high concentration of oxygen

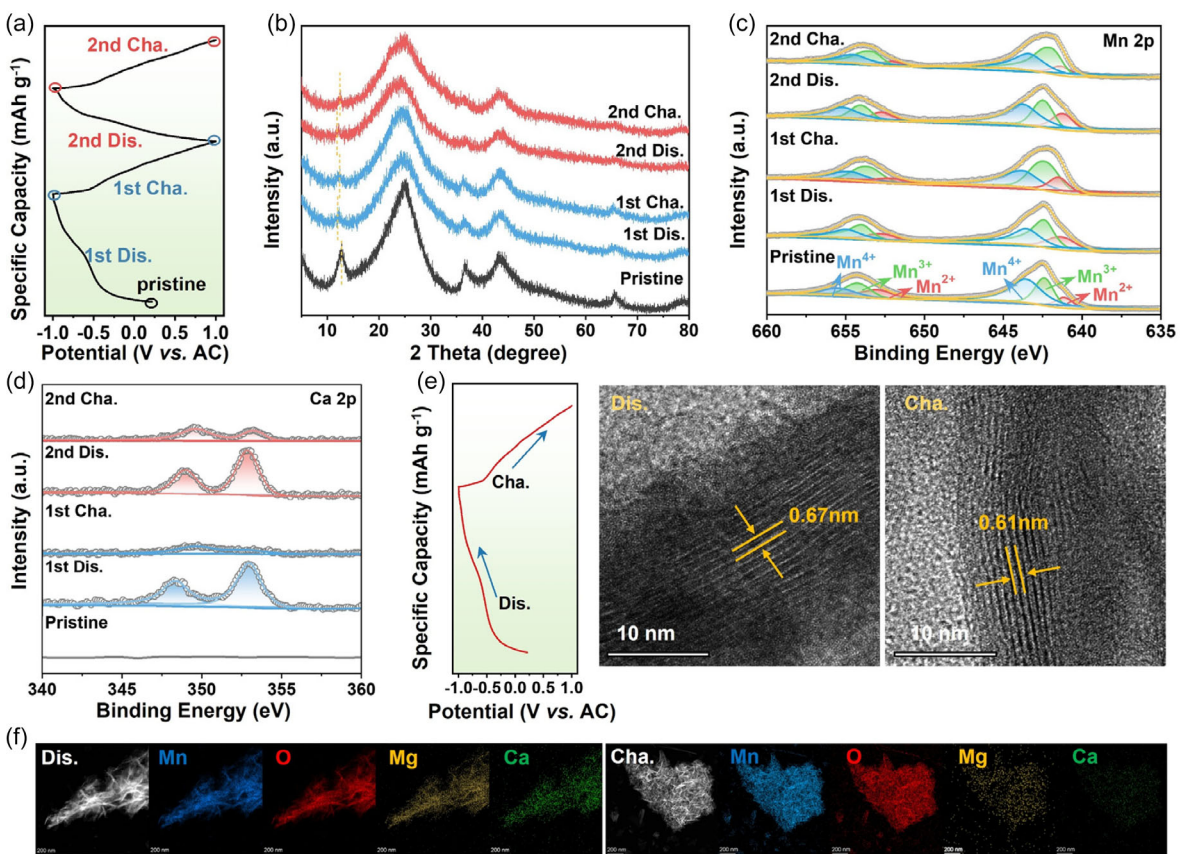


Figure 5. a) The GCD curves for the first two cycles at 0.1 A g^{-1} and the corresponding b) ex situ XRD patterns, c) Mn 2p and d) Ca 2p XPS spectra of MMO-2 electrodes at different charge/discharge states. e,f) The GCD curves for the first cycle at 0.1 A g^{-1} and the corresponding HRTEM images and EDS mappings of MMO-2 at discharged and charged states.

vacancies exhibits fast electrochemical reaction kinetics. As a result, the optimized MMO electrode exhibits the highest reversible specific capacity (458.2 mAh g⁻¹ at 0.1 A g⁻¹), superior rate capability (164.2 mAh g⁻¹ at 1 A g⁻¹), and cycling stability (a capacity retention rate of 99.3% after 1000 cycles at 1.0 A g⁻¹). Furthermore, the reaction mechanism of H⁺ and Ca²⁺ cointercalation in the MMO electrode has been revealed through ex situ experimental tests. This work provides a defect-engineering strategy for the design of high-performance cathode materials.

Acknowledgements

G.L. and W.H. contributed equally to this work. This work was financially supported by National Natural Science Foundation of China (52173091) and Department of Science and Technology of Hubei Province (2024CSA076).

Conflict of Interest

The authors declare no conflict of interest.

Data Availability Statement

The data that support the findings of this study are available from the corresponding author upon reasonable request.

Keywords: alzheimer's disease • amyloid-β • membrane-like environment • oxidative stress • redox active metals

- [1] Y. Wu, Z. Zhao, X. Hao, R. Xu, L. Li, D. Lv, X. Huang, Q. Zhao, Y. Xu, Y. Wu, *Carbon Neutral*. **2023**, *2*, 551.
- [2] C. M. Costa, J. C. Barbosa, R. Gonçalves, H. Castro, F. J. D. Campo, S. Lanceros-Méndez, *Energy Storage Mater.* **2021**, *37*, 433.
- [3] J. Sun, J. Li, T. Zhou, K. Yang, S. Wei, N. Tang, N. Dang, H. Li, X. Qiu, L. Chen, *Nano Energy* **2016**, *27*, 313.
- [4] X. Yu, A. Manthiram, *Chem* **2018**, *4*, 1200.
- [5] H. Bu, H. Lee, J. Hyoung, J. W. Heo, D. Kim, Y. J. Lee, S.-T. Hong, *Chem. Mater.* **2023**, *35*, 7974.
- [6] A. Ponrouch, M. R. Palacin, *Curr. Opin. Electrochem.* **2018**, *9*, 1.
- [7] L. Yan, W. Yang, H. Yu, L. Zhang, J. Shu, *Energy Storage Mater.* **2023**, *60*, 102822.
- [8] X. Deng, L. Li, G. Zhang, X. Zhao, J. Hao, C. Han, B. Li, *Energy Storage Mater.* **2022**, *53*, 467.
- [9] B. W. Byles, N. K. R. Palapati, A. Subramanian, E. Pomerantseva, *APL Mater.* **2016**, *4*, 046108.
- [10] M. H. Alfaruqi, S. Islam, V. Mathew, J. Song, S. Kim, D. P. Tung, J. Jo, S. Kim, J. P. Baboo, Z. Xiu, J. Kim, *Appl. Surf. Sci.* **2017**, *404*, 435.
- [11] X. Zhu, Z. Cao, W. Wang, H. Li, J. Dong, S. Gao, D. Xu, L. Li, J. Shen, M. Ye, *ACS Nano* **2021**, *15*, 2971.
- [12] Q. Zhao, A. Song, S. Ding, R. Qin, Y. Cui, S. Li, F. Pan, *Adv. Mater.* **2020**, *32*, e2002450.
- [13] J. Huang, Z. Wang, M. Hou, X. Dong, Y. Liu, Y. Wang, Y. Xia, *Nat. Commun.* **2018**, *9*, 2906.
- [14] Y. Xu, G. Zhang, J. Liu, J. Zhang, X. Wang, X. Pu, J. Wang, C. Yan, Y. Cao, H. Yang, W. Li, X. Li, *Energy Environ. Mater.* **2023**, *6*, e12575.
- [15] C. Zuo, F. Xiong, Y. Shao, M. Li, D. Zhu, J. Zhu, J. Wang, Q. An, *Energy Storage Mater.* **2024**, *72*, 103763.
- [16] C. Zuo, F. Xiong, J. Wang, Y. An, L. Zhang, Q. An, *Adv. Funct. Mater.* **2022**, *32*, 2202975.
- [17] Y. Wu, K. Zhang, S. Chen, Y. Liu, Y. Tao, X. Zhang, Y. Ding, S. Dai, *ACS Appl. Energy Mater.* **2019**, *3*, 319.
- [18] J. Wang, J. G. Wang, X. Qin, Y. Wang, Z. You, H. Liu, M. Shao, *ACS Appl. Mater. Interface* **2020**, *12*, 34949.
- [19] M. H. Alfaruqi, S. Islam, J. Gim, J. Song, S. Kim, D. T. Pham, J. Jo, Z. Xiu, V. Mathew, J. Kim, *Chem. Phys. Lett.* **2016**, *650*, 64.
- [20] X. Xia, Y. Zhao, Y. Zhao, M. Xu, W. Liu, X. Sun, *Nano Res.* **2022**, *16*, 2511.
- [21] Y. Zhao, S. Zhang, Y. Zhang, J. Liang, L. Ren, H. J. Fan, W. Liu, X. Sun, *Energy Environ. Sci.* **2024**, *17*, 1279.
- [22] H. Li, H. Wang, M. Yang, Y. Sun, Y. Yin, P. Guo, *Colloids Surf., A* **2020**, *602*, 125068.
- [23] Q. Xie, G. Cheng, T. Xue, L. Huang, S. Chen, Y. Sun, M. Sun, H. Wang, L. Yu, *Mater. Today Energy* **2022**, *24*, 100934.
- [24] W. Zhao, J. Fee, H. Khanna, S. March, N. Nisly, S. J. B. Rubio, C. Cui, Z. Li, S. L. Suib, *J. Mater. Chem. A* **2022**, *10*, 6762.
- [25] G. G. Yadav, J. W. Gallaway, D. E. Turney, M. Nyce, J. Huang, X. Wei, S. Banerjee, *Nat. Commun.* **2017**, *8*, 14424.
- [26] S. Abbas, T. H. Bokhari, A. Zafar, S. Javed, S. Karim, H. Sun, S. Hussain, A. Khalid, Y. Yu, R. T. A. Khan, I. Ullah, A. Nisar, M. Ahmad, *J. Energy Storage* **2024**, *87*, 111455.
- [27] N. Zarshad, A. U. Rahman, J. Wu, A. Ali, F. Raziq, L. Han, P. Wang, G. Li, H. Ni, *Chem. Eng. J.* **2021**, *415*, 128967.
- [28] N. Liang, X. Sun, L. Qi, S. Zhang, L. Lin, C. Dong, X. Wang, *Energy Technol.* **2022**, *10*, 2200502.
- [29] W. Zhao, J. Fee, H. Khanna, S. March, N. Nisly, S. J. B. Rubio, C. Cui, Z. Li, S. L. Suib, *J. Mater. Chem. A* **2022**, *10*, 6762.
- [30] J. Xia, Y. Zhou, J. Zhang, T. Lu, W. Gong, D. Zhang, X. Wang, J. Di, *Small* **2023**, *19*, e2301906.
- [31] M. Xu, Y. Cai, T. Wang, X. Wang, A. Zhou, Z. Yang, *J. Alloys Compd.* **2021**, *877*, 160243.
- [32] T. Li, N. Zhang, B. Liu, P. Wang, Z. Liu, Y. Wang, D. Xu, H. Tian, Q. Zhang, T. F. Yi, *Adv. Funct. Mater.* **2025**, *32*, 2423755.
- [33] Z. Pan, L. Jin, C. Yang, X. Ji, M. Liu, *Chem. Eng. J.* **2023**, *470*, 144084.
- [34] G. Zhao, J. Li, L. Jiang, H. Dong, X. Wang, W. Hu, *Chem. Sci.* **2012**, *3*, 433.
- [35] Y. Chen, C. Lin, X. Chen, Z. Lu, K. Zhang, Y. Liu, J. Wang, G. Han, G. Xu, *Adv. Energy Mater.* **2024**, *14*, 2304303.
- [36] S. Chen, Y. Kong, C. Tang, N. A. Gadelhak, A. K. Nanjundan, A. Du, C. Yu, X. Huang, *Small* **2024**, *20*, e2312229.
- [37] J. Zhao, X. Liu, P. Liu, K. Deng, X. Lv, W. Tian, C. Wang, S. Tan, J. Ji, *J. Colloid Interface Sci.* **2023**, *629*, 1039.
- [38] A. Xia, C. Zhao, W. Yu, Y. Han, J. Yi, G. Tan, *J. Appl. Electrochem.* **2020**, *50*, 733.
- [39] S. O. Choi, M. Penninger, C. H. Kim, W. F. Schneider, L. T. Thompson, *ACS Catal.* **2013**, *3*, 2719.
- [40] Y. Li, W. Zhang, Y. Zheng, J. Chen, B. Yu, Y. Chen, M. Liu, *Chem. Soc. Rev.* **2017**, *46*, 6345.
- [41] Y. Wang, H. Quan, Q. Zhang, B. Tan, W. Chen, D. Chen, *ACS Appl. Nano Mater.* **2024**, *7*, 27988.
- [42] S. Liu, H. Huang, C. Yang, Y. Liu, H. Li, H. Xia, T. Qin, J. Zhou, X. Liu, *Chem. Eng. J.* **2022**, *441*, 135967.
- [43] J. Han, D. S. Li, L. Jiang, D. N. Fang, *Adv. Sci.* **2022**, *9*, e2105510.
- [44] K. Ma, S. Ge, R. Fu, C. Feng, H. Zhao, X. Shen, G. Liang, Y. Zhao, Q. Jiao, *Chem. Eng. J.* **2024**, *484*, 149525.
- [45] L. Yan, L. Niu, C. Shen, Z. Zhang, J. Lin, F. Shen, Y. Gong, C. Li, X. Liu, S. Xu, *Electrochim. Acta* **2019**, *306*, 529.
- [46] P. Xu, H. Yi, G. Shi, Z. Xiong, Y. Hu, R. Wang, H. Zhang, B. Wang, *Dalton Trans.* **2022**, *51*, 4695.
- [47] S. Yao, R. Zhao, S. Wang, Y. Zhou, R. Liu, L. Hu, A. Zhang, R. Yang, X. Liu, Z. Fu, D. Wang, Z. Yang, Y.-M. Yan, *Chem. Eng. J.* **2022**, *429*, 132521.
- [48] Y. Zou, W. Zhang, N. Chen, S. Chen, W. Xu, R. Cai, C. L. Brown, D. Yang, X. Yao, *ACS Nano* **2019**, *13*, 2062.
- [49] F. Xu, Z. Shi, J. Wu, H. Liu, J. Li, F. Zan, H. Xia, *J. Power Sources* **2024**, *602*, 234342.
- [50] Z. Qin, Y. Song, Y. Liu, X.-X. Liu, *Chem. Eng. J.* **2023**, *451*, 138681.
- [51] C.-F. Wang, S.-W. Zhang, L. Huang, Y.-M. Zhu, F. Liu, J.-C. Wang, L.-M. Tan, C.-Y. Zhi, C.-P. Han, *Rare Met.* **2024**, *43*, 2597.

- [52] X. Qin, X. Zhao, G. Zhang, Z. Wei, L. Li, X. Wang, C. Zhi, H. Li, C. Han, B. Li, *ACS Nano* **2023**, *17*, 12040.
- [53] F. Qiao, J. Wang, R. Yu, Y. Pi, M. Huang, L. Cui, Z. Liu, Q. An, *Small Methods* **2024**, *8*, e2300865.
- [54] X. Zhao, L. Li, L. Zheng, L. Fan, Y. Yi, G. Zhang, C. Han, B. Li, *Adv. Funct. Mater.* **2023**, *34*, 2309753.
- [55] K. Lu, B. Song, Y. Zhang, H. Ma, J. Zhang, *J. Mater. Chem. A* **2017**, *5*, 23628.
- [56] X. Yang, W. Deng, M. Chen, Y. Wang, C. F. Sun, *Adv. Mater.* **2020**, *32*, e2003592.

Manuscript received: April 30, 2025
Revised manuscript received: July 7, 2025
Version of record online:
